International Journal of Heat and Fluid Flow 103 (2023) 109175

Contents lists available at ScienceDirect

International Journal of Heat and Fluid Flow

journal homepage: www.elsevier.com/locate/ijhff

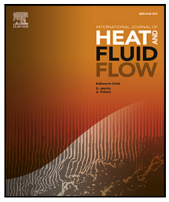

# POD analysis of the turbulent boundary layer flow downstream of miniature vortex generators

C.I. Chan *, R.C. Chin

*School of Electrical and Mechanical Engineering, University of Adelaide, South Australia 5005, Australia*

ARTICLE INFO

*Keywords:*
Turbulent boundary layer
Miniature vortex generator
Proper orthogonal decomposition

ABSTRACT

In this study we investigate the influence of an array of miniature vortex generators (MVGs) in a zero-pressure-gradient turbulent boundary layer (ZPG TBL) by means of a large-eddy simulation of rectangular MVGs in a spatially evolving moderate Reynolds number ZPG TBL up to $Re_\tau = 1350$. The MVG array consists of pairs of rectangular blades arranged in spanwise oriented arrays in the flow. The turbulent intensities and streamwise inclination angles related to the large streamwise extent high-momentum regions (HMRs) and low-momentum regions (LMRs) induced by the MVGs are presented. The instantaneous velocity fluctuation is decomposed into a turbulent velocity component and a spatial velocity component based on the triple velocity decomposition, where the spatial velocity component represents a spatial variation of the time-averaged flow induced by the MVGs. The streamwise turbulent velocity fluctuation associated with the HMRs and the LMRs is further investigated using proper orthogonal decomposition (POD), where we further examine a reduced-order reconstruction of the HMRs and the LMRs, using two-dimensional data. POD has also been used to determine the streamwise inclination angle of wall-attached structures in the HMRs and the LMRs. An examination of the streamwise inclination angle associated with the POD modes has been performed. Results suggest that the streamwise inclination angle of higher energy POD modes may be related to that of the relatively large wall-attached structures reported in the literature. In addition, if the lower energy POD modes are also retained, the value of the streamwise inclination angle tends to approach the value of mean streamwise inclination angle of wall-attached structures. The results suggest that the decreasing trend in streamwise inclination angle may be related to the contributions of the small-scale wall-attached motions.

## 1. Introduction

The miniature vortex generator (MVG) is a passive flow control device that can generate streamwise-oriented vortices, leading to long and persistent streamwise streaks that evolve downstream in boundary layer flows. Due to its simplicity and cost-effectiveness, MVG continues to be considered a promising solution for effective flow control. The effects of a MVG array on laminar boundary layers developing on flat plates have been investigated experimentally and numerically and are comprehensively understood (Lin, 2002; Fransson and Talamelli, 2012; Shahinfar et al., 2012). It is widely recognised that they can delay flow transition from laminar to turbulent by stabilising the growth of Tollmien–Schlichting waves and oblique disturbances, leading to significant skin friction reduction (Fransson et al., 2006; Fransson and Talamelli, 2012; Shahinfar et al., 2012, 2014; Sattarzadeh et al., 2014).

Recent experimental and numerical studies (Lögdberg et al., 2009; Chan and Chin, 2021) were conducted to investigate the turbulent flow control by vortex generators in the zero-pressure-gradient turbulent boundary layer (ZPG TBL). Although the same skin friction reduction effects (laminar boundary layer flows) were not observed in fully turbulent boundary layer flows, the studies demonstrated that the induced high-momentum regions and low-momentum regions (HMRs and LMRs) are able to persist for up to $300h$ (where $h$ is the device height) in moderate Reynolds number ZPG TBLs. We have adopted a canonical case similar to Lögdberg et al. (2009) by simplifying the flow geometry as a ZGP TBL over a flat plate (see Chan and Chin, 2021). This simplified flow situation allows us to focus on the underlying flow physics to a greater extent in comparison to more complex practical flow scenarios (adverse pressure gradients). Nevertheless, it is crucial to be aware of such differences and exercise caution when interpreting the results based on the present ZPG investigation, as the findings may be influenced to some extent by the pressure gradient.

The coherent motions in smooth-wall-bounded turbulent boundary layer flows are well established to be related to turbulence generation and energy transport (Robinson, 1991; Smits et al., 2011). The near-wall turbulence is well understood to be related to the formation of

* Corresponding author.
*E-mail address:* chiip.chan11@gmail.com (C.I. Chan).

https://doi.org/10.1016/j.ijheatfluidflow.2023.109175
Received 12 January 2023; Received in revised form 11 May 2023; Accepted 8 June 2023
Available online 21 June 2023

quasi-streamwise vortices and streamwise streaks by the self-sustained mechanisms (Hamilton et al., 1995; Jiménez and Pinelli, 1999; Panton, 2001; Guerrero et al., 2022). These naturally occurring streamwise-elongated high- and low-momentum regions occupy the logarithmic region of the turbulent boundary layer (Tomkins and Adrian, 2003; Hutchins and Marusic, 2007a). Very-large-scale motions or large-scale streamwise elongated modes have been found to exist far away from the wall, and they influence the near-wall turbulence with increasing Reynolds numbers (Hutchins and Marusic, 2007b; Mathis et al., 2009). Previous studies have demonstrated that many of these coherent motions are inclined at an angle with respect to the mean flow direction. The cross-correlation between the fluctuating wall-shear stress and the fluctuating streamwise velocity in the logarithmic region has long been used to infer the mean streamwise inclination angle (SIA) of the coherent motions in this region. This angle is defined in the average sense, where coherent motions with different length scales are assumed to be convecting across the logarithmic region at the same time (Marusic and Heuer, 2007; Deshpande et al., 2019; Cheng et al., 2022).

Compared to the previously mentioned characteristics regarding the coherent motions in smooth-wall ZPG TBLs, ZPG TBLs with emerged vortices, such as those generated by low-profile or miniature vortex generators (with ratios $h/\delta \leq 0.2$, where $\delta$ is the 99% boundary layer thickness), exhibit organised HMRs and LMRs that propagate downstream up to $300h$ (Lögdberg et al., 2009; Chan and Chin, 2021, 2022). These organised HMRs and LMRs are distinct from those observed in smooth-wall cases and are remarkably similar to the high-momentum pathways and low-momentum pathways found in spanwise heterogeneous rough-wall bounded flows. The high- and low-momentum pathways in spanwise heterogeneous rough-wall bounded flows, characterised by the counter-rotating swirling motions, have been extensively studied through numerous experimental and numerical investigations (e.g. Barros and Christensen, 2014; Anderson et al., 2015). These pathways have been shown to be associated with the spanwise alternating high- and low-wall-shear stress regions, where upwelling and downwelling motions occur above the high- and low-wall-shear stress regions, respectively. The occurrence of streamwise roll motions has been attributed to the sharp gradient in the shear stress from the high-shear stress region to the low-shear stress region in the spanwise direction, which is controlled by the roughness spacings (Chung et al., 2018). This phenomenon is similar to the behaviours observed in flows with MVG arrays, where the sizes and spacings of the induced vortices and the associated HMRs and LMRs are strongly influenced by the MVG spacings (Chan and Chin, 2021, 2022). Therefore, studying the streamwise evolution and behaviour of the HMRs and the LMRs in more detail would be worthwhile.

The effect of MVGs on the mean structural inclination angle of the coherent motions, as observed in the high- and low-wall-shear stress regions, in comparison to a smooth-wall ZPG TBL without MVGs, is still uncertain. A better understanding of these parameters could help in the development of efficient approaches for simulating turbulent boundary layers with emerged vortex models. For instance, Lögdberg et al. (2009) proposed the pseudo-viscous vortex model, which uses the potential flow theory to explain the vortex evolution and development generated by the MVGs. Mole et al. (2022), based on the Batchelor vortex model, studied a computationally efficient approach for accurately representing the downstream interaction between the vortex pairs and the boundary layer without directly resolving the geometry of the vortex generators (VGs).

The present study focuses on the HMRs and the LMRs in turbulent boundary layers induced by MVGs. Our analysis is based on a large-eddy simulation data set of a MVG array placed in a turbulent boundary layer at a moderate Reynolds number. The velocity fluctuation fields of the HMRs and the LMRs are analysed based on the triple decomposition to investigate the coherent and turbulent velocity fluctuations. To identify the most energetic coherent motions in these regions, we use the proper orthogonal decomposition (POD) technique. This approach enables us to identify the dominant flow patterns (eigenvectors) and the associated energy contents (eigenvalues) based on the streamwise turbulent kinetic energy norm. Additionally, we will utilise POD to investigate the inclination angles of large- and small-scale coherent motions. The second objective of the present study is to investigate the influence of a MVG array on the SIA of the large-scale motions in the HMRs and the LMRs extracted by the POD. Assessing the SIA of coherent motions in the logarithmic region is of great practical importance for evaluating the attached-eddy framework and developing near-wall turbulence models (Marusic and Monty, 2019). In the following, Section 2 describes the numerical procedure employed for the simulation. In Section 3 and Section 3.1, the influence of the MVGs on the HMRs and the LMRs is discussed, and a further analysis of the HMRs and the LMRs based on the POD is presented. The influence of the MVGs on the SIA is presented in Section 4, and the POD is then extended to provide further discussion on the streamwise inclination angles of the large- and small-scale motions in Section 5. Conclusions are presented in Section 6.

## 2. Numerical procedure

In the following, the streamwise, wall-normal and spanwise coordinates are denoted as $x$, $y$ and $z$, respectively. Their instantaneous velocity components are denoted by $u$, $v$ and $w$, respectively. The time-averaged velocity is denoted by the $(\bar{\cdot})$ or the capital letter e.g. $\overline{u} = U$, and its (turbulent) fluctuation is denoted by the prime $(\cdot')$. The symbol $\langle\bar{\cdot}\rangle$ denotes the spanwise and temporal average, i.e.

$$\langle\overline{q}\rangle(x,y) = \frac{1}{L_z}\int_{L_z}\overline{q}(x,y,z)\,\mathrm{d}z, \tag{1}$$

where $L_z$ denotes the total width of the MVG array. A large-eddy simulation of an array of MVGs set up in a moderate Reynolds number ZPG TBL was performed. The simulation setup was motivated by recent experimental studies of Lögdberg et al. (2009), Sattarzadeh et al. (2014) and Sattarzadeh and Fransson (2015). The configuration of MVG pairs is shown in Fig. 1. The array of MVGs is positioned at $x_{\mathrm{M}} = 950\delta_0^*$ from the inlet (corresponding to $Re_\tau = \delta^+ \simeq 430$, where $\delta_0^*$ is the inlet displacement thickness). The parameters of a MVG when scaled by the inlet displacement thickness, are respectively: $h = 4$ is the blade height, $t_m = 1$ is the blade thickness, $L = 10$ is the blade length, $d = 10$ is the spanwise distance between the centroids of blades in one pair. $\Lambda_z = 40$ is the spanwise spacing between two adjacent MVG pairs. $\alpha = 15°$ denotes the angle of attack of the MVG with respect to the inlet flow direction. The large-eddy simulation was performed using a fully spectral numerical code (Chevalier et al., 2007). A sub-grid-scale approximate deconvolution model (ADM-RT) has been employed to compute approximations to the unfiltered solutions of the incompressible continuity and Navier–Stokes equations by a repeated filter operation, i.e.

$$\frac{\partial\hat{u}_i}{\partial x_i} = 0, \tag{2}$$

$$\frac{\partial\hat{u}_i}{\partial t} + \hat{u}_j\frac{\partial\hat{u}_i}{\partial x_j} + \frac{\partial\hat{p}}{\partial x_i} - \frac{1}{Re}\frac{\partial^2\hat{u}_i}{\partial x_j\partial x_j} = -\chi H_N \circledast \hat{u}_i, \tag{3}$$

with superscripts $\wedge$ refer to a resolved-scale, and $\circledast$ denotes the convolution and the relaxation term $-\chi H_N \circledast \hat{u}_i$ : $\chi$ is the model coefficient; and $H_N \circledast \hat{u}_i$ is the high-pass approximately deconvolved quantities. The ADM-RT model has been widely used for performing incompressible transitional and turbulent flows simulations (Stolz et al., 2001; Schlatter et al., 2004; Eitel-Amor et al., 2014; Schlatter et al., 2010). Spatial discretisation is based on a Fourier series with 3/2 zero-padding for de-aliasing in the streamwise $(x)$ and spanwise $(z)$ directions, and a Chebyshev polynomial is employed in the wall-normal direction $(y)$. The computational domain in the streamwise, wall-normal and spanwise directions are respectively: $x_L \times y_L \times z_L = 6000\delta_0^* \times 200\delta_0^* \times 360\delta_0^*$ using $6144 \times 513 \times 768$ spectral modes. This give uniform grid spacings

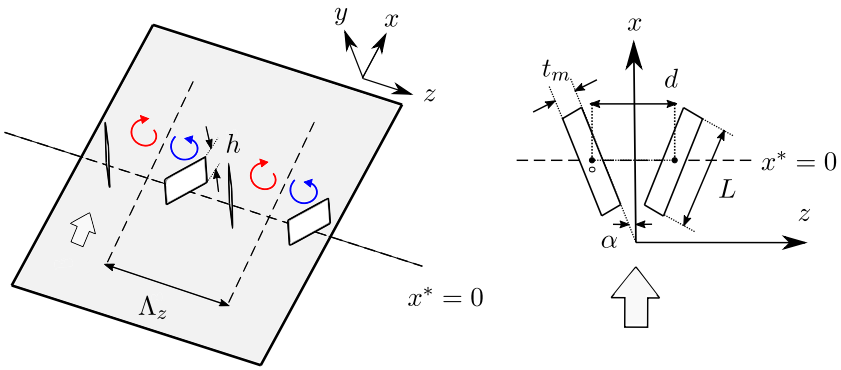


**Fig. 1.** Schematic of the MVG layouts considered in the present study. The parameters of a MVG are scaled by the inlet displacement thickness $\delta_0^*$: $h = 4$ is the blade height, $t_m = 1$ is the blade width, $L = 10$ is the blade length, $\alpha = 15°$ is the angle of attack of the MVG with respect to the flow direction, $d = 10$ is the spanwise distance between the centroids of blades in a MVG pair and $\Lambda_z = 40$ is the spanwise spacing between two different MVG pairs.

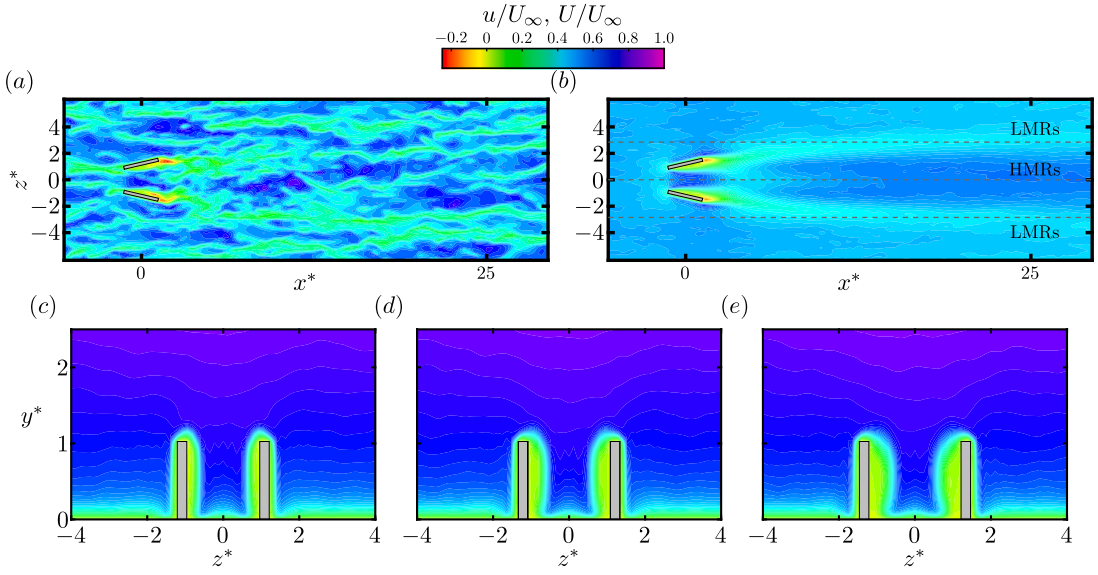


**Fig. 2.** (*a*) Instantaneous realisation of the streamwise velocity flow field, $u/U_\infty$, at $y^* = 0.25$ past a MVG pair. Top view (*b*) and cross-section views of the time-averaged streamwise velocity flow field, $U/U_\infty$, at (*c*) $x^* = -0.5$, (*d*) $x^* = 0$ and (*e*) $x^* = 0.5$, where $x^* = (x - x_M)/h$, $x_M$ is defined at the centre of the MVG array and $z^* = z/h$. Rectangular box outlines the MVG cross section. In (*b*), the dashed black lines mark the spanwise locations of the HMRs and the LMRs, with secondary flows of common flow down and common flow up at $x^* = 25$, respectively. The rectangular boxes are not to scale.

of $\Delta x^+ \approx 16.9$ and $\Delta z^+ \approx 8.1$ in the streamwise and spanwise directions (the superscript + refers to scaling with the friction velocity $u_\tau = \sqrt{\tau_w/\rho}$ and kinematic viscosity $\nu$, where $\tau_w$ is the wall shear stress and $\rho$ is the fluid density). In the wall-normal direction, there is a minimum of 15 Chebyshev collocation points within the region $y^+ < 10$. The first grid point away from the wall is at $y^+ \approx 0.03$, and the maximum spacing is $\Delta y^+_{\max} = 10.6$. The time advancement is carried out by a second-order Crank–Nicolson scheme for the viscous terms and a third-order four-stage Runge–Kutta scheme for the non-linear terms (Chevalier et al., 2007). Details on the numerical procedure for the simulation can be found in Chan and Chin (2021) and Chan and Chin (2022).

## 3. High- and low-momentum regions

Fig. 2 illustrates the effects of the MVG array in a TBL with instantaneous and time-averaged streamwise velocity fields obtained in the streamwise–spanwise plane at $y/h = y^* = 0.25$ (Figs. 2*a* and 2*b*), and spanwise-wall-normal plane at $x^* = -0.5$, 0 and 0.5 of the time-averaged streamwise velocity field (Figs. 2*c*, 2*d* and 2*e*), where $x^* = (x - x_M)/h$ is defined at the centre of a blade. Spanwise alternating high- and low-speed patterns are clearly observed with HMRs formed along the centrelines of the MVGs and LMRs formed in the regions adjacent to the HMRs.

The mean and turbulent statistics of the HMRs and the LMRs are first presented before we investigate the associated SIA based on the POD. The mean flow and streamwise stresses of the HMRs and the LMRs are shown in Fig. 3. Fig. 3(*a*) shows the differences of the time-averaged streamwise velocity between the HMRs and the LMRs. Here, the global TBL is the spanwise and temporal average as defined in (1). The velocity defect in the mean flow profile can be estimated by comparing the downward or upward shift of the log-law constants with the reference case without a MVG array, i.e. a smooth-wall DNS TBL mean velocity profile is utilised as the reference case (Chan et al., 2021), which is shown as the dashed black line with a constant of $B = 5.2$. The vertical solid line denotes the wall-normal location $y^* \simeq 0.5\,(y^+ = 2h^+)$, which yields $\Delta U^+ = -1.5$ at the LMRs (blue line) and $\Delta U^+ = 1.0$ at the HMRs (red line), respectively. The velocity defect is related to the local skin friction variation, where locally the skin friction is modified over the HMRs and the LMRs along the spanwise direction. The low-speed fluid is lifted from the wall and reduces the streamwise wall shear stress $\tau_w$ and results in a substantial local skin friction drag reduction (with respect to the case without a MVG array). On the other hand, the downwash motion transports the high-speed fluid from the outer region towards the wall and increases the local skin friction drag at the centre of the MVG pair. Fig. 3(*b*) shows the velocity perturbation

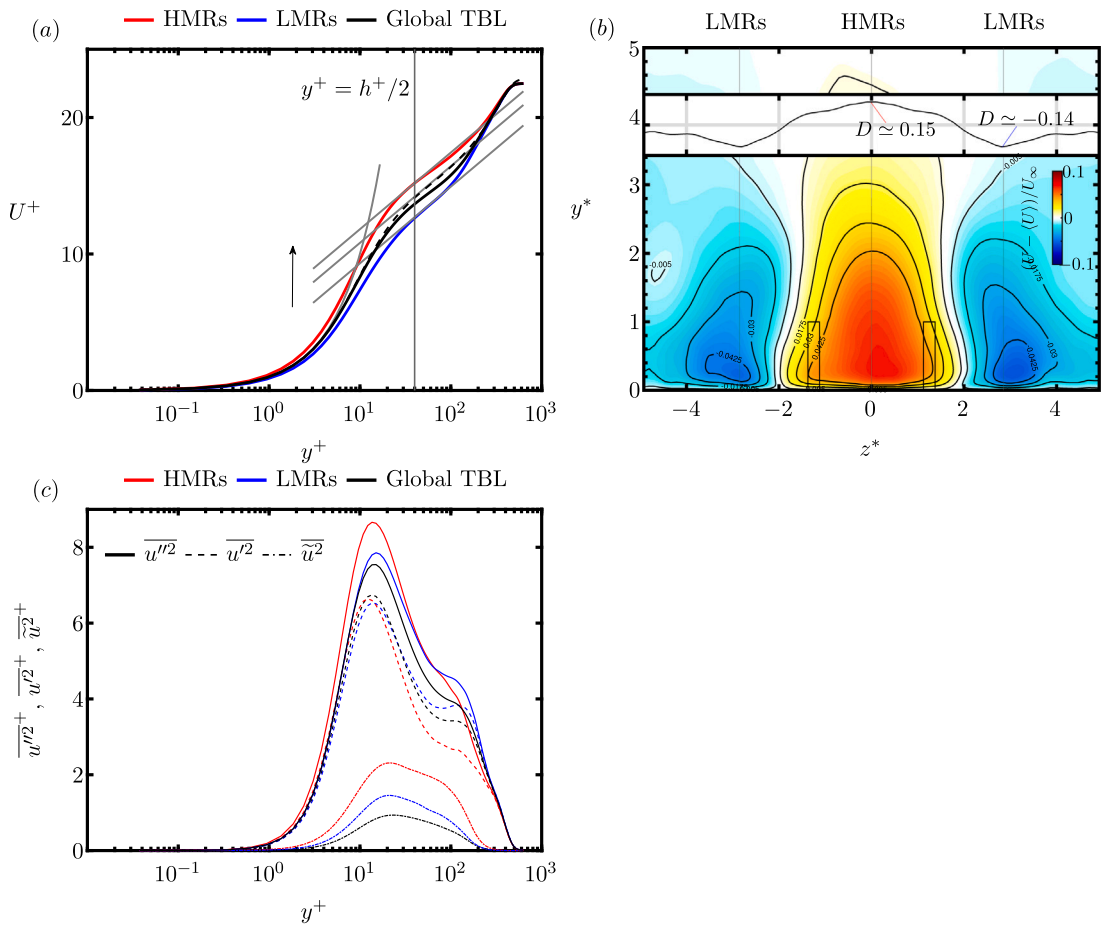


**Fig. 3.** (*a*) Comparison of the time-averaged streamwise velocity at $x^* = 25$. The thick grey lines denote the linear and log-law regions $1/\kappa \log y^+ + B$ with $\kappa = 0.41$ and $B = 3.7$, 5.2 and 6.2 in the arrow direction. The smooth-wall DNS TBL mean velocity profile is utilised as the reference case and is shown as the dashed black line with a constant of $B = 5.2$. (*b*) The velocity excess $(U - \langle U \rangle)/U_\infty > 0$ associated with the high-speed region and the velocity deficit $(U - \langle U \rangle)/U_\infty < 0$ associated with the low-speed region at $x^* = 25$. Inset shows the local spanwise skin friction variation at $x^* = 25$. (*c*) Comparison of the (time-averaged) streamwise stresses: $\overline{u''^2}$, $\overline{u'^2}$ and $\overline{\widetilde{u}^2}$.

defined as $(U - \langle U \rangle)/U_\infty$, indicating the locations of the HMRs and the LMRs and showing the presence of the streamwise roll-modes induced downstream of the MVG array. The inset in Fig. 3(*b*) shows the local spanwise skin friction variation at $x^* = 25$, defined as $D(x, z^*) = (\bar{\tau}_w - \bar{\tau}_{w,0})/\bar{\tau}_{w,0}$, where $\bar{\tau}_w = \nu (d\bar{u}/dy)|_{y=0}$ is the time-averaged wall shear stress and $z^* = z/h$. The $\bar{\tau}_{w,0}$ refers to the smooth-wall reference case. The $D > 0$ denotes the local drag increase and $D < 0$ denotes the local drag reduction. The inset plot suggests that the HMRs are associated with increases of skin friction up to $D \simeq 0.15$ at $z^* = 0$, accompanied with similar skin friction reduction rates centred at the LMRs (up to $D \simeq -0.14$ at $z^* \simeq \pm 3$).

The drag behaviour and the secondary flow patterns observed in the Fig. 3(*a*, *b*) demonstrate that MVGs are capable of providing sufficient momentum transfer away and towards the wall over a downstream region that is in the order of the device height, with a much lower device drag compared to conventional VGs (Lin, 2002). This makes MVGs suitable for flow control applications where a boundary layer flow redistribution is required. MVG can generate pairs of counter-rotating streamwise vortices that are just strong enough to redistribute fluids without persisting unnecessarily within the boundary layer once the flow control objective is achieved (Lin, 2002). Furthermore, the MVGs create pairs of counter-rotating vortices that quickly merge to form a single secondary flow pattern that remains close to the wall in the thin region of the boundary layer. This induced secondary flow pattern can be applied to reduce flow distortion, for example, inlet flow distortion observed in compact S-ducts (Lin, 2002).

To further elucidate the physical modification of MVGs on the turbulent statistics, we employed a triple decomposition of the velocity components, which reads as:

$$u_i(x, y, z, t) = \langle U_i \rangle(x, y) + u_i'(x, y, z, t) + \widetilde{u}_i(x, y, z), \tag{4}$$

where the $u_i'$ and $\widetilde{u}_i$ on the right-hand side of Eq. (4) are the turbulent fluctuations and MVG-induced fluctuations, respectively. The MVG-induced fluctuations, $\widetilde{u}_i = U_i - \langle U_i \rangle$, are the spatial variation of the time-averaged flow due to MVG. The total fluctuations, $u_i'' = u_i' + \widetilde{u}_i$, equal to the turbulent fluctuations $(u_i')$ for the smooth-wall case since $\widetilde{u}_i = 0$. The streamwise total stress $(\overline{u''u''})$, the Reynolds stress $(\overline{u'u'})$ and the MVG-induced stress $(\overline{\widetilde{u}\widetilde{u}})$ are presented in Fig. 3(*c*) for the HMRs, LMRs and global TBL. The comparison of the profiles of the MVG-induced stress (represented by red and blue dotted-dash lines) over the HMRs and the LMRs indicates that the modification of turbulent flow intensities by the MVGs on the HMRs is distinct from that on the LMRs. This is further evidenced by the differences observed in the turbulent stress (red and blue dash lines) of these regions.

In the following section, we will delve into this observation in greater detail. We will conduct further assessments of the HMRs and the LMRs based on the POD, which will include a low-order reconstruction of the turbulent fluctuations in the HMRs and the LMRs, as well as an analysis of the SIA that is associated with the wall-attached structures in the HMRs and the LMRs.

### 3.1. POD analysis of HMRs and LMRs

The POD method with an energy-based norm is a useful tool for decomposing the velocity fluctuation field into sets of POD modes and expansion coefficients. This decomposition provides important spatial and temporal information about the dominant coherent motions in the flow (Rowley et al., 2004). POD is used in this section to investigate the turbulent velocity fluctuations associated with the HMRs and the LMRs. In this study, the number of spatial points in the numerical simulation data set is larger than the number of snapshots available. Therefore, the snapshot POD approach has been used and will be briefly described here. Practically, the streamwise turbulent fluctuation is approximated by a finite sum of expansion coefficients $a_i$ and spatial modes $\phi_i$ as:

$$u'(\boldsymbol{x},t) \simeq \sum_{i=1}^{N} a_i(t)\boldsymbol{\phi}_i(\boldsymbol{x}). \tag{5}$$

The spatial modes $\boldsymbol{\phi}_i(\boldsymbol{x})$ were obtained from solving an eigenvalue problem of the correlation matrix of $u'$. The correlation matrix was calculated between individual snapshots of streamwise velocity fluctuation, $u'(\boldsymbol{x},t_i) = u'(\boldsymbol{x},t_1), u'(\boldsymbol{x},t_2), \ldots$, based on their temporal correlations. The correlation (temporal) matrix is given by:

$$\boldsymbol{M} = M_{ij} = \frac{1}{N_t - 1}\left[u'(\boldsymbol{x},t_i), u'(\boldsymbol{x},t_j)\right]_D, \tag{6}$$

where $N_t$ denotes the total number of snapshots and $[\cdot]_D$ defines the inner product. The eigenvalue problem to be solved can be written as:

$$\boldsymbol{M}\boldsymbol{\psi}_i = \lambda_i \boldsymbol{\psi}_i. \tag{7}$$

The eigenvalues might be sorted in a descending order to relate to the energy content of the corresponding modes. Because we solve the eigenvalue problem based on temporal correlations, we need to project all the eigenmodes $\boldsymbol{\psi}_i$ to the velocity field $u'(\boldsymbol{x},t_i)$ to recover the first $N_t$ spatial POD modes as

$$\boldsymbol{\phi}_j(\boldsymbol{x}) = \frac{\sum_i \psi_j(t_i)u'(\boldsymbol{x},t_i)}{\sqrt{\lambda_j}\sqrt{N_t - 1}}, \tag{8}$$

where the spatial POD modes are essentially orthonormal, i.e. $[\boldsymbol{\phi}_i, \boldsymbol{\phi}_j]_D = \delta_{ij}$. Finally, the expansion coefficients $a_i$ can be obtained by projection of the velocity field on the spatial modes. In the following, we will consider the two-dimensional POD modes and examine the correlation in the spanwise direction for $u'(y, |z^*| \le 5, t)$., i.e.

$$u'(y,z,t) \simeq \sum_{i=1}^{N} a_i(t)\phi_i(y,z). \tag{9}$$

The first six POD modes $\phi_i(y,z)$ are presented in Fig. 4. The POD modes are ranked according to the magnitudes of their eigenvalues. The first POD mode appears to be anti-correlated in between the HMRs and the LMRs, clearly reflecting the symmetrical streamwise vortices pairs appearing downstream of the MVG array. A visual inspection of the spanwise separation between the correlation regions of same sign implies that $\lambda_z \simeq \Lambda_z/2$. This is consistent with the spanwise wavelength of the energy peak at the dominant spanwise mode as observed in Chan and Chin (2021), even though the first POD mode itself contributes to only 6% of the total energy (Fig. 5). The percentage contributions to the total energy of the POD modes are plotted in Fig. 5. It can be seen that the contribution of the first six POD modes to the total energy is approximately 25% and is up to 80% for the first $10^2$ POD modes. A low-order reconstruction has been commonly used to provide an approximation of the dominant coherent motions in fluid flows (Rowley et al., 2004; Mohammed-Taifour and Weiss, 2016). By reconstructing the velocity fluctuation field from the low-order POD modes, an approximation of the dominant motions in the HMRs and the LMRs can be identified and a comparison between their turbulence intensities can be performed. Fig. 6 shows the low-order reconstructions of the streamwise turbulent intensity in the HMRs ($z^* = 0$) and the LMRs ($z^* \simeq -3$) obtained using 2D POD modes,

$$u' \sim u'_{N_R}(\boldsymbol{x},t) = \sum_{i=1}^{N_R} a_i(t)\boldsymbol{\phi}_i(\boldsymbol{x}), \tag{10}$$

where $N_R = 1, 2, \ldots$, denotes the number of POD modes for reconstruction. Results show that the first $10^2$ modes reconstruction is a fairly good approximation of the intensity profile, where they contribute to almost 80% of the total energy (as shown in Fig. 5), and,

$$\frac{[u'_{N_R}(\boldsymbol{x},t_i), u'_{N_R}(\boldsymbol{x},t_i)]_D}{[u'(\boldsymbol{x},t_i), u'(\boldsymbol{x},t_i)]_D} = \sum_{i}^{N_R}\lambda_i / \sum_{i}^{N}\lambda_i, \tag{11}$$

where $\overline{a_i(t)a_j(t)} = \lambda_i\delta_{ij}$. Fig. 6 also demonstrates how the reconstructed intensity profiles vary with increasing number of modes, particularly at the near-wall peak $y^+ \simeq 15$ and outer region $y/\delta \simeq 0.2$ ($y^+ \simeq 120$). It can be seen that the outer peaks for both the HMRs and the LMRs are clearly associated with the first few dominant POD modes. The inner peaks seem to shift towards $y^+ \simeq 15$ when higher modes are included in the reconstruction. The red dashed line in Fig. 6($a$) suggests that $u'_{N_R=1} \simeq 0$. This is attributed to $Re[\phi_1(y, z^* = 0)] \simeq 0$ as shown in Fig. 4 (illustrated as vertical dashed line in Fig. 4). On the other hand, the vertical solid line in Fig. 4 represents the reconstruction of the LMRs based on $\phi_1(y, z^* = -3)$, plotted as intensity profile in Fig. 6($b$) (red dashed line). The first few modes also exhibit alternating spatial patterns with opposite sign spaced in the spanwise direction, where the HMRs and the LMRs are localised at the interface between these patterns. This indicates that the reconstructed velocity fluctuations associated with the HMRs and the LMRs are anti-correlated.

## 4. Influence on the mean streamwise inclination angle

The influence of MVGs on the mean streamwise inclination angle, SIA, of the coherent motions in the HMRs and the LMRs is investigated in this section. The SIA characterises the mean structure inclination angle of the wall-attached energy-containing motions, which are believed to be populated in the logarithmic and outer regions where they are rooted in the near-wall region and inclined at an angle to the mean flow direction (Marusic and Heuer, 2007; Deshpande et al., 2019). The SIA is typically obtained by deducing the local maximum value of the streamwise cross-correlation function between the streamwise velocity fluctuation ($u'$) at a wall-normal position in the log region ($y_o$) and the streamwise wall-shear stress fluctuation ($\tau'_w$) (Marusic and Heuer, 2007; Deshpande et al., 2019; Cheng et al., 2022). The streamwise cross-correlation function can be expressed as

$$R_{\tau u}(x,y,\Delta x) = \frac{\langle \overline{\tau'_w(x,z)u'(x+\Delta x,y,z)}\rangle}{\sqrt{\langle\overline{\tau'^2_w}\rangle}\sqrt{\langle\overline{u'(x,y)^2}\rangle}}, \tag{12}$$

where $\langle\cdot\rangle$ denotes the temporal and spanwise ensemble average. The SIA can be obtained by

$$\theta^w_m = \arctan\left(\frac{y_o}{\Delta x_p(y_o)}\right), \tag{13}$$

where $\Delta x_p$ is the streamwise delay at the local maximum value of $R_{\tau u}$,

$$\Delta x_p(y_o) = \left|\arg\max_{\Delta x} R_{\tau u}(x,y_o,\Delta x)\right|, \tag{14}$$

where $y^+_o = 2.6\sqrt{Re_\tau}$ is used in the present study as the wall-normal position of log-region (Marusic et al., 2013). The SIA is typically inferred as the mean structural inclination angle contributed by different range of scales of energy-containing wall-attached motions (Deshpande et al., 2019; Cheng et al., 2022). The reported range of the SIA in the literature is approximately from 12° to 16° (Marusic and Heuer, 2007). In addition to the mean structural inclination angle, Deshpande et al. (2019) reported that the structure inclination angle for the large-scale

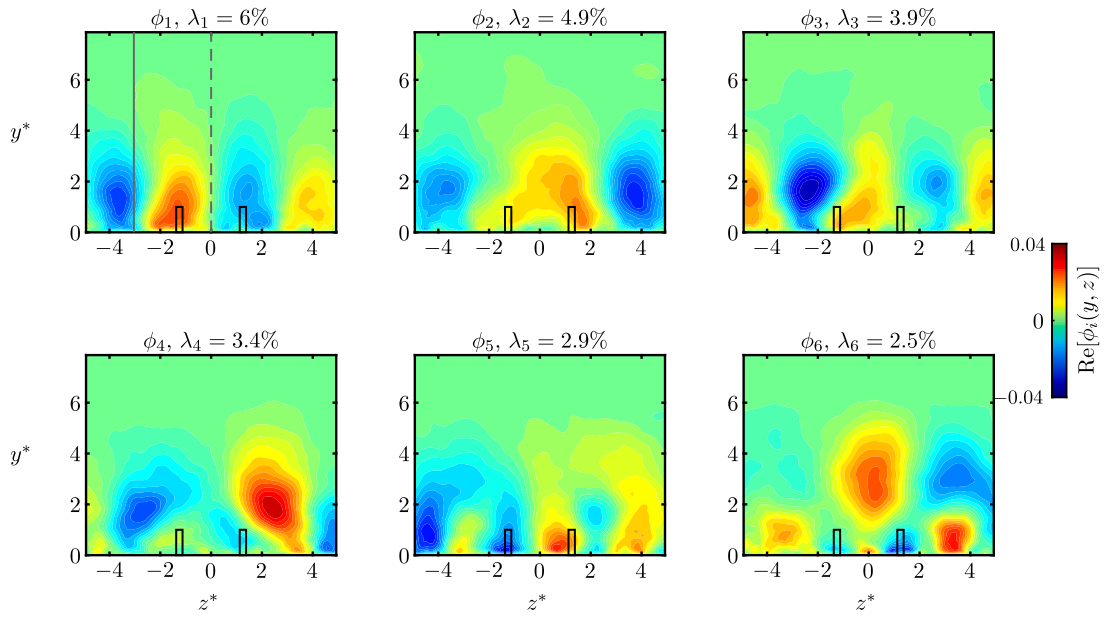


**Fig. 4.** The first six two-dimensional POD modes $\phi_i(y,z)$ with their eigenvalues ranked by their percentage contributions. Re[·] denotes real part of the complex number.

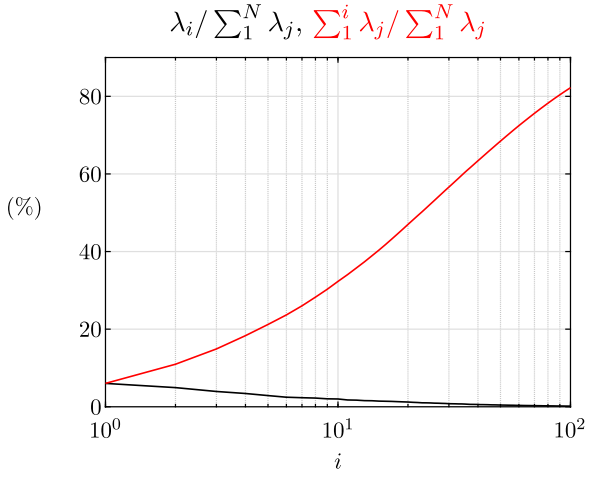


**Fig. 5.** The percentage contribution of the eigenvalues (black ——) and cumulative sum of the eigenvalues (red ——) for two-dimensional POD modes. (For interpretation of the references to colour in this figure legend, the reader is referred to the web version of this article.)

wall-attached motions in the logarithmic region is approximately 45° to the wall, which is obtained by introducing spanwise offsets in the probe measurements to separate the relatively small-scale wall-attached motions.

Fig. 7 shows the streamwise cross-correlation function $R_{\tau u}$ for HMRs, LMRs and global TBL at $x^*/h = 25$, at $x^*/h = 500$ and the respective SIA values at various downstream locations. From Figs. 7(*a*) and 7(*b*), the correlation contour levels between the HMRs and the LMRs appear distinguishable at $x^*/h = 25$ with little overlap of contour levels between the HMRs and the LMRs, while at $x^*/h = 500$ where the flow motions are expected to be spanwise homogeneous, the contour levels between the HMRs and the LMRs are well overlapped. Overall, the results indicate that the HMRs and the LMRs are similar in terms of SIA, which is evident in Fig. 7(*c*). From Fig. 7(*c*), the difference in the values of SIA between the HMRs and the LMRs is negligible, and there is no significant variation in the SIA with increasing $x^*/h$ or Reynolds number. This suggests that a Reynolds number dependence of the SIA is not observed. This is consistent with the Reynolds number invariance of the SIA reported for smooth-wall ZPG TBLs at similar Reynolds numbers (Marusic and Heuer, 2007).

## 5. POD modes-reconstructed inclination angle

To provide additional clarity on the influence of large- and small-scale motions on the SIA obtained in the previous section, we perform a calculation of the SIA utilising the POD technique. In Section 4, the mean structure inclination angle, SIA, computed from (12)–(14) is the mean angle based on a range of different scales of wall-attached motions. The POD has been used as a tool of capturing energy (i.e. as defined by the induced norm) in the velocity fluctuating fields by expressing the velocity fluctuation with a superposition of POD modes, and the average energy content of each mode is denoted by its corresponding eigenvalue (Rowley et al., 2004). Based on this idea, the contribution of each POD mode to the cross-correlation function can be assessed accordingly from (10). If we consider a time series data, in this case we first redefine the cross-correlation function in the form (Marusic and Heuer, 2007):

$$R_{u_r u}(y,z,\Delta t) = \frac{\langle \overline{u'(y_r,z,t)u'(y,z,t+\Delta t)} \rangle}{\sqrt{\langle \overline{u'(y_r)^2} \rangle}\sqrt{\langle \overline{u'(y)^2} \rangle}}, \tag{15}$$

where the near-wall location $y_r^+ \simeq 0.03$ is used. Inserting Eq. (10) into (15) gives

$$R_{u_r u}(y,z,\Delta t) \simeq \frac{\langle \overline{u'(y_r,z,t)u'_{N_R}(y,z,t+\Delta t)} \rangle}{\sqrt{\langle \overline{u'(y_r)^2} \rangle}\sqrt{\langle \overline{u'_{N_R}(y)^2} \rangle}}, \tag{16}$$

where (16) may then be rewritten in terms of POD modes that are ranked according to the eigenvalue in descending order: $\lambda_1 > \lambda_2 > \lambda_3 > \ldots$:

$$R_{u_r u}(y,z,\Delta t) \simeq \sum_{i=1}^{N_R} \mathcal{R}_i(y,z,\Delta t) = \mathcal{R}_1^{N_R}(y,z,\Delta t), \tag{17}$$

i.e. the near-wall streamwise velocity fluctuation $u_r$ is correlated with each of the POD mode. The methodology is different from where we decompose both $u_r$ and $u$ and the correlation of each POD mode with itself will only be considered in this case because of orthonormality. Therefore, from (17), the $\mathcal{R}_i^{N_R}(y,z,\Delta t)$ can be interpreted as the reconstruction to the cross-correlation function by the energy captured by the POD modes $i$ to $N_R$, at locations $y$, $z$ with time delay $\Delta t$.

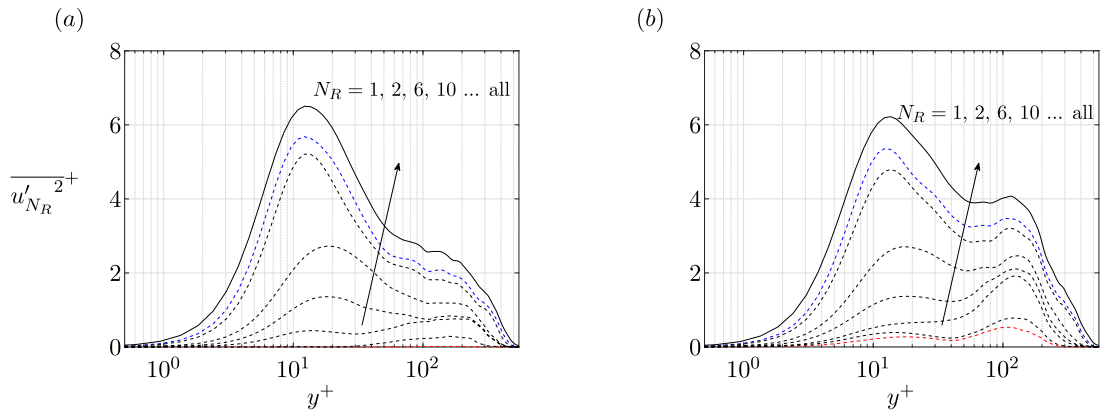


**Fig. 6.** Low-order reconstructions of streamwise turbulent stress using the first $N_R$ two-dimensional POD modes: $N_R = 1$ (red dashed line), 100 (blue dashed line), 2, 6, 10, 20, 60 (black dashed lines) in the arrow direction and using all modes (solid line)(*a*) HMRs and (*b*) LMRs. (For interpretation of the references to colour in this figure legend, the reader is referred to the web version of this article.)

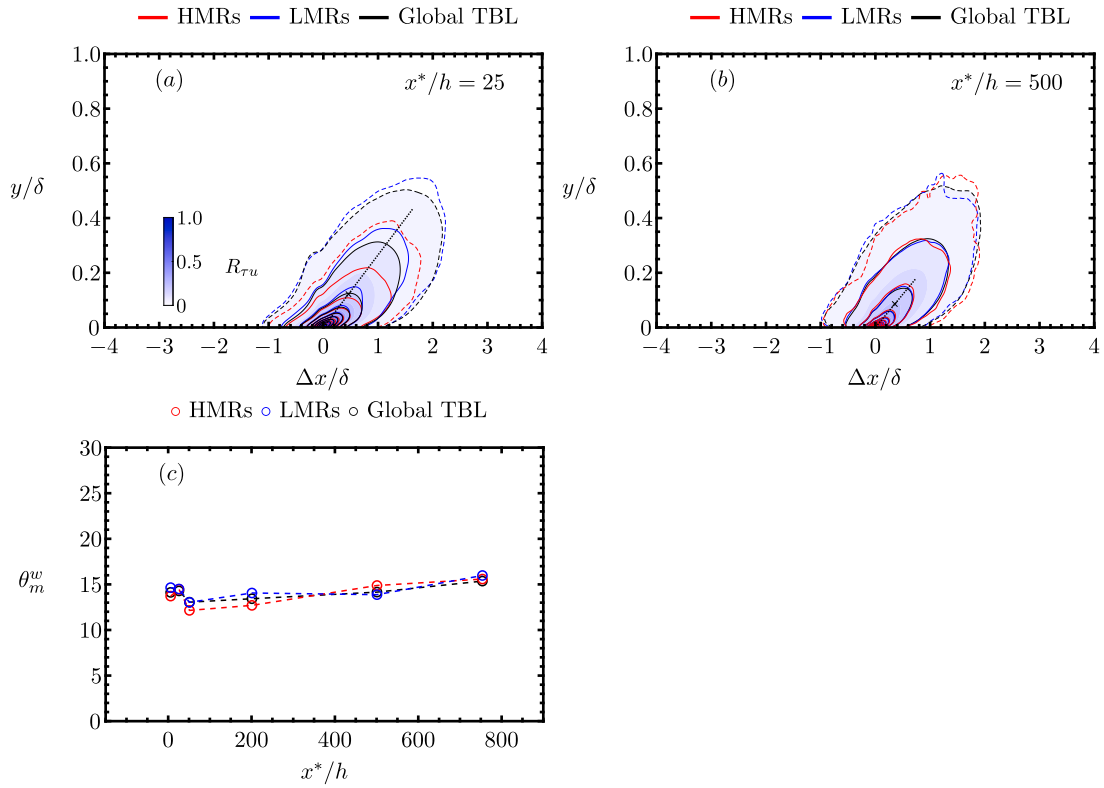


**Fig. 7.** Influence of MVGs on the mean streamwise inclination angles. $(a, b)$ The streamwise cross-correlation $R_{\tau u}$, computed based on the streamwise velocity fluctuation $u'$ and streamwise wall shear stress fluctuation $\tau'_w$ for different wall-normal locations. The dotted line in $(a, b)$ denotes the SIA and the symbol × intercepting with the inclination line marks the wall-normal position in the log-region where $y^+_o = 2.6\sqrt{Re_\tau}$ and the corresponding streamwise delay. Iso-lines are: 0.05 (outermost dash line) and [0.1 : 0.1 : 1] (solid line). The colour contour is at levels [0 : 0.05 : 1] for the global TBL. $(c)$ The evolution of SIA, $\theta^w_m$ at different streamwise locations downstream of the MVGs. (For interpretation of the references to colour in this figure legend, the reader is referred to the web version of this article.)

Fig. 8$(a, b)$ presents the normalised temporal correlation functions reconstructed by different numbers of POD modes (normalised by their maximum values, $R_{u_\tau u,max}$ and $\mathcal{R}^{N_R}_{i,max}$, respectively). Here the spanwise location is limited to $|z^*| \leq 5$. Fig. 8$(a)$ presents the normalised temporal cross-correlation function when only the high-energy rank POD modes are retained, i.e. the POD modes with high eigenvalues. We observe that when we include the first $10^3$ POD modes we can reconstruct a very similar correlation function, i.e. $\mathcal{R}^{10^3}_1 \simeq R_{u_\tau u}$. It is not surprising because we have shown in Fig. 5$(b)$ that the first $10^2$ POD modes have captured more than 80% of the energy, while the first $10^3$ POD modes have captured almost all the energy. Moreover, from Fig. 8$(a)$ (from left to right), it is observed that the peak of the correlation is gradually shifted away from the wall when excluding more and more low-energy rank POD modes, exhibiting a roughly constant time shift from the near-wall region. The peak is reflecting the first and second POD modes in Fig. 4, which are peaked at $y^+ \simeq 1.5h^+ = 120$ away from the wall. This confirms that the high-energy rank POD modes not only contribute to the correlation function in the logarithmic region, but also with non-negligible contributions to the wall. We also look into the contribution from the low-energy rank POD modes. From (17), it can be computed as the subtraction: $\mathcal{R}^{N_R}_j(\Delta t) = \mathcal{R}^{N_R}_1 - \mathcal{R}^{j-1}_1$ for $j > 1$, which eliminates the POD modes from $i = 1$ to $i = j - 1$. Fig. 8$(b)$ is evident that the low-energy rank POD modes reassemble the near wall contribution to the correlation function. The inset in Fig. 8$(b)$

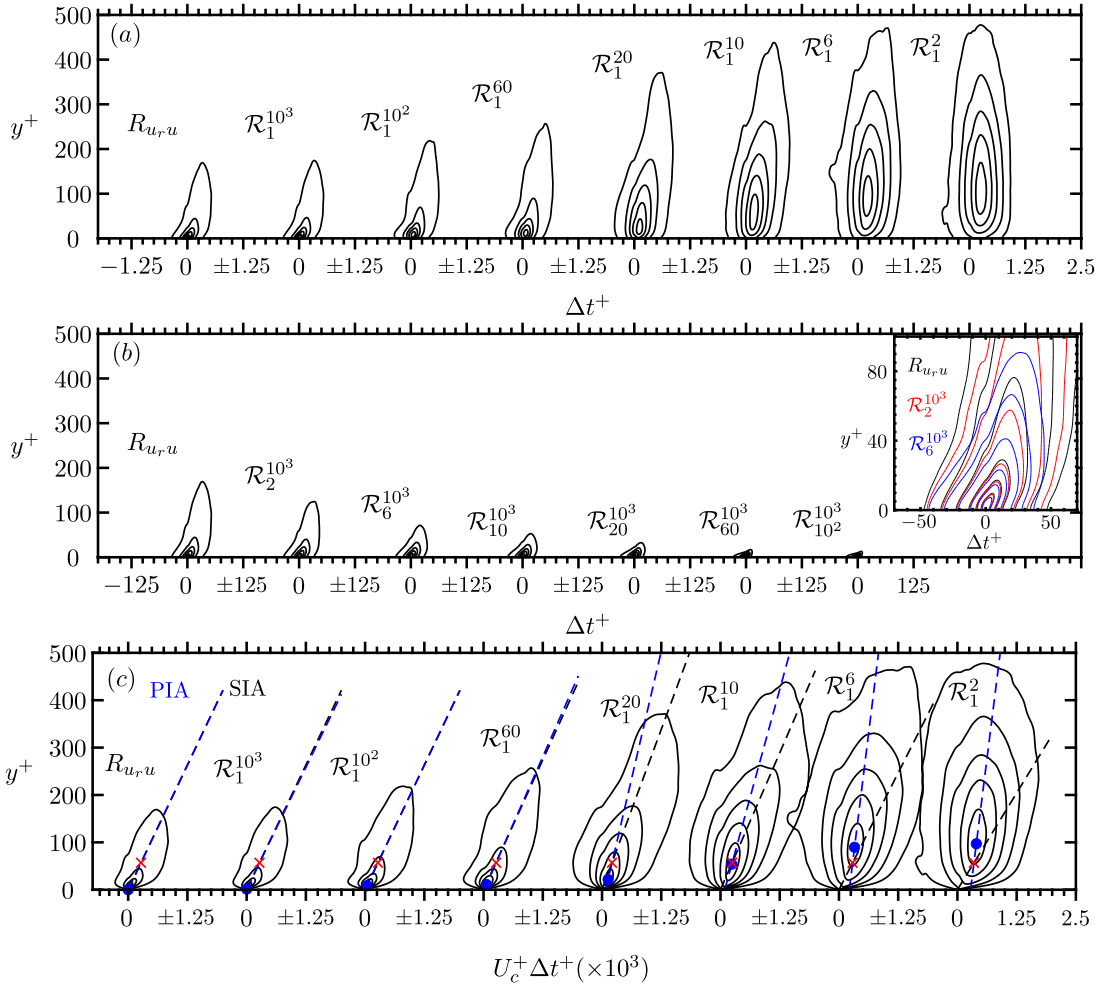


**Fig. 8.** Normalised temporal cross-correlation functions $R_{u_ru}(\Delta t^+)$ and normalised POD-mode dependent cross-correlation functions $\mathcal{R}_i^{N_R}(\Delta t^+)$ (normalised by their respective maximum values, $R_{u_ru,max}$ and $\mathcal{R}_{i,max}^{N_R}$, normalised contour levels are at [0.1 : 0.2 : 1]). $(a, b)$ Temporal delay $(\Delta t^+)$ is estimated based on the time series data at $x^*/h = 25$. Inset in $(b)$ is the comparison of the actual values (without normalisation with their maximum values) of the temporal cross-correlation functions $R_{u_ru}(\Delta t^+)$ (black), $\mathcal{R}_2^{10^3}(\Delta t^+)$ (red) and $\mathcal{R}_6^{10^3}(\Delta t^+)$ (blue). The contours are at levels [0.05, 0.1, 0.2 : 0.2 : 1]. $(c)$ The corresponding streamwise delay of $(a)$. The streamwise delay is constructed based on the Taylor's hypothesis ($\Delta x^+ = U_c^+\Delta t^+$). Here the local mean velocity is used as the convection velocity $U_c^+(y^+) = U^+(y^+)$. The SIA is marked by black dash line. The PIA is marked by blue dash line. The red (×) symbols mark the wall-normal locations: $y_o^+ = 2.6\sqrt{Re_\tau}$. The blue filled circles mark the global peak locations. (For interpretation of the references to colour in this figure legend, the reader is referred to the web version of this article.)

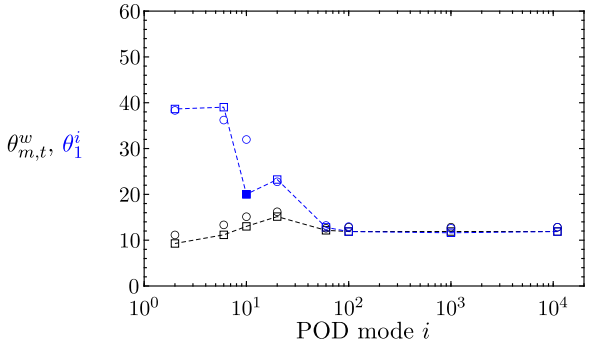


**Fig. 9.** Summary of two streamwise inclination angles with number of POD modes employed. The mean streamwise inclination angle (SIA, $\theta_{m,t}^w$, black coloured symbols) and POD modes-dependent inclination angle (PIA, $\theta_1^i$, blue coloured symbols). Reference wall-normal locations of logarithmic region: $y_o^+ = 2.6\sqrt{Re_\tau} \simeq 0.12Re_\tau$ (square), $y_o^+ = 0.15Re_\tau$ (circle). (For interpretation of the references to colour in this figure legend, the reader is referred to the web version of this article.)

shows the comparison of the actual values (without normalisation with their maximum values) of the temporal cross-correlation functions $R_{u_ru}$ (black), $\mathcal{R}_2^{10^3}$ (red) and $\mathcal{R}_6^{10^3}$ (blue). It is seen that when the first few POD modes are removed (first mode in $\mathcal{R}_2^{10^3}$ and first five modes in $\mathcal{R}_6^{10^3}$), the correlation contour in the outer part of the plot decreases considerably, while the near-wall correlation is slightly affected. The observations suggest that the near-wall correlation is mainly ascribed to the contributions of the low-energy rank POD modes and they have relatively small time delays from inspecting the correlation maps in Fig. 8$(a, b)$ (or streamwise delays as $\Delta t \propto \Delta x$ at particular $y$). On the other hand, the high-energy rank POD modes mainly contribute to the outer correlation and they have relatively large time and streamwise delays.

To characterise the inclination angle for the correlation functions reconstructed by the POD modes, we will use two definitions: the first definition of the streamwise inclination angle is defined similar to the SIA, where

$$\theta_{m,t}^w = \arctan\left(\frac{y_o^+}{\Delta x_p^+}\right), \tag{18}$$

$$\Delta t_p = \left|\arg\max_{\Delta t} \mathcal{R}_i^{N_R}(y_o, \Delta t)\right|, \tag{19}$$

where Taylor's frozen turbulence hypothesis is used here to construct a streamwise delay $\Delta x_p^+ = U_c^+(y_o^+)\Delta t_p^+$ from the temporal cross-correlation

function. In this approximation, the convection velocity is assumed to be the local mean velocity, i.e. $U_c^+(y_o^+) = U^+(y_o^+)$. The second definition of the streamwise inclination angle is obtained by locating the best-fitted line of local maximum value at the assumed logarithmic region ($y_o^+ = 2.6\sqrt{Re_\tau}$) to the global peak at $y_g$ and $\Delta t_g$ where

$$(y_g, \Delta t_g) = \left| \arg\max_{y,\Delta t} \mathcal{R}_i^{N_R}(y, \Delta t) \right|, \tag{20}$$

$$\theta_1^i = \arctan\left( \left| \frac{y_o^+ - y_g^+}{\Delta x_g^+} \right| \right), \tag{21}$$

where $\Delta x_g^+ = U_c^+(y_o^+)\Delta t_p^+ - U_c^+(y_g^+)\Delta t_g^+$. This angle can be interpreted as how the streamwise delay at the local maximum is varied with respect to the change in the number of POD modes involved in the logarithmic region (where we assumed at $y_o^+$). Therefore, we denote the second streamwise inclination angle as POD modes-dependent inclination angle (PIA). It can also be seen that by definition, the PIA is essentially the SIA when the global peak is attached at the wall (i.e. $y_g^+ \simeq 0$, $\Delta t_g^+ \simeq 0$). Fig. 8($c$) shows the reconstruction of streamwise delays of Fig. 8($a$) using the Taylor's hypothesis. The two different inclination angles, SIA and PIA, are illustrated in Fig. 8($c$), plotted as black and blue dash lines, respectively.

Fig. 9 summarises the PIA and the SIA versus the number of POD modes as shown in Fig. 8($c$). The figure shows that SIA and PIA exhibit very different trends when fewer high-energy rank POD modes are retained (square symbols). The PIA of the first two POD modes is about 38°. This value is similar to the reported value of the SIA of large wall-attached structures in the literature (e.g. Deshpande et al., 2019; Cheng et al., 2022). As the number of POD modes increases, the PIA decreases gradually from 38° and agrees better with the SIA. When all the modes are considered, the PIA and SIA agrees well with the results in the literature, i.e. $\theta_{m,t}^{w} \simeq 12° - 14°$, where a small variation as shown here is likely attributed to the choice of $y_o^+$ and the choice of convection velocity employed in the Taylor's hypothesis. For example, a limitation of the present definition of PIA is that when the value of $y_o^+$ is very similar to the value of $y_g^+$ as illustrated in Fig. 8($c$) (the $\mathcal{R}_1^{10}$), the assessed PIA appears as a outlier point as shown in Fig. 9 (blue filled square at $i = 10$). We have checked the sensitivity of the presented results to the reference wall-normal location of logarithmic region ($y_o^+$). Fig. 9 suggests that a similar trend is observed with a different choice of $y_o^+$, but for this $y_o^+$, the outlier point disappears. Therefore, a careful selection of $y_o$ is needed.

## 6. Conclusion

In this study we focused on the flow behaviour of the long streamwise extended and spanwise periodic HMRs and LMRs induced by a MVG array. A large-eddy simulation data set of rectangular MVGs positioned in a spatially evolving moderate Reynolds number ZPG TBL up to $Re_\tau = 1350$ was utilised (Chan and Chin, 2021). The fluctuating velocity fields associated with the HMRs and the LMRs are first extracted by a triple velocity decomposition, and the streamwise velocity fluctuation is analysed using POD in the spanwise and wall-normal directions. The POD analysis showed that spanwise correlation characterises the main difference between the HMRs and the LMRs in the low-order velocity reconstruction. Results showed that the first few 2D POD modes have similar alternating spatial patterns with opposite sign spaced in the spanwise direction, where the HMRs and the LMRs are localised at the interface between these regions, suggesting that their streamwise velocity fluctuations are anti-correlated. POD analysis has also been incorporated in the examination of the streamwise inclination angles of wall-attached structures. The streamwise inclination angle associated with the POD modes, PIA, has been assessed (Figs. 8 and 9). When fewer high-energy POD modes are retained, the PIA tends to approach the value of streamwise inclination angle of relatively large wall-attached structures reported in the literature, i.e. ∼45°, whilst when more POD modes are retained, the PIA tends to decrease to the value of SIA of the wall-attached structures, i,e. ∼14°. The decreasing trend of the PIA is thus believed to be related to the contributions of low-energy POD modes capturing the small-scale wall-attached motions.

## CRediT authorship contribution statement

**C.I. Chan:** Conceptualization, Methodology, Writing – original draft. **R.C. Chin:** Conceptualization, Supervision, Writing – review & editing.

## Declaration of competing interest

The authors declare that they have no known competing financial interests or personal relationships that could have appeared to influence the work reported in this paper.

## Data availability

Data will be made available on request.

## Acknowledgements

The authors acknowledge the financial support of the Australian Research Council. This work was supported with supercomputing resources provided by the Phoenix HPC service at the University of Adelaide, Australia. Research was also undertaken with the assistance of resources provided at the NCI NF through the Computational Merit Allocation Scheme, supported by the Australian Government and the Pawsey Supercomputing Centre, with funding from the Australian Government and the Government of Western Australia.

## References

Anderson, W., Barros, J.M., Christensen, K.T., Awasthi, A., 2015. Numerical and experimental study of mechanisms responsible for turbulent secondary flows in boundary layer flows over spanwise heterogeneous roughness. J. Fluid Mech. 768, 316–347. http://dx.doi.org/10.1017/jfm.2015.91.

Barros, J.M., Christensen, K.T., 2014. Observations of turbulent secondary flows in a rough-wall boundary layer. J. Fluid Mech. 748, R1. http://dx.doi.org/10.1017/jfm.2014.218.

Chan, C.I., Chin, R.C., 2021. Investigation of the influence of miniature vortex generators on the large-scale motions of a turbulent boundary layer. J. Fluid Mech. 932, A29. http://dx.doi.org/10.1017/jfm.2021.1013.

Chan, C.I., Chin, R.C., 2022. Decomposition of the Reynolds shear stress in a turbulent boundary layer modified by miniature vortex generators. Phys. Rev. Fluids 7, 054603. http://dx.doi.org/10.1103/PhysRevFluids.7.054603.

Chan, C.I., Schlatter, P., Chin, R.C., 2021. Interscale transport mechanisms in turbulent boundary layers. J. Fluid Mech. 921, A13. http://dx.doi.org/10.1017/jfm.2021.504.

Cheng, C., Shyy, W., Fu, L., 2022. Streamwise inclination angle of wall-attached eddies in turbulent channel flows. J. Fluid Mech. 946, A49. http://dx.doi.org/10.1017/jfm.2022.657.

Chevalier, M., Lundbladh, A., Henningson, D.S., 2007. SIMSON–A pseudo-spectral solver for incompressible boundary layer flow. Tech. Rep. TRITA-MEK 2007:07, Citeseer, KTH Mechanics, Stockholm, Sweden..

Chung, D., Monty, J.P., Hutchins, N., 2018. Similarity and structure of wall turbulence with lateral wall shear stress variations. J. Fluid Mech. 847, 591–613. http://dx.doi.org/10.1017/jfm.2018.336.

Deshpande, R., Monty, J.P., Marusic, I., 2019. Streamwise inclination angle of large wall-attached structures in turbulent boundary layers. J. Fluid Mech. 877, R4. http://dx.doi.org/10.1017/jfm.2019.663.

Eitel-Amor, G., Örlü, R., Schlatter, P., 2014. Simulation and validation of a spatially evolving turbulent boundary layer up to $Re_\theta = 8300$. Int. J. Heat Fluid Flow (ISSN: 0142-727X) 47, 57–69. http://dx.doi.org/10.1016/j.ijheatfluidflow.2014.02.006.

Fransson, J.H.M., Talamelli, A., 2012. On the generation of steady streamwise streaks in flat-plate boundary layers. J. Fluid Mech. 698, 211–234. http://dx.doi.org/10.1017/jfm.2012.80.

Fransson, J.H.M., Talamelli, A., Brandt, L., Cossu, C., 2006. Delaying transition to turbulence by a passive mechanism. Phys. Rev. Lett. 96, 064501. http://dx.doi.org/10.1103/PhysRevLett.96.064501.

Guerrero, B., Lambert, M.F., Chin, R.C., 2022. Precursors of backflow events and their relationship with the near-wall self-sustaining process. J. Fluid Mech. 933, A33. http://dx.doi.org/10.1017/jfm.2021.1082.

Hamilton, J.M., Kim, J., Waleffe, F., 1995. Regeneration mechanisms of near-wall turbulence structures. J. Fluid Mech. 287, 317–348. http://dx.doi.org/10.1017/S0022112095000978.

Hutchins, N., Marusic, I., 2007a. Evidence of very long meandering features in the logarithmic region of turbulent boundary layers. J. Fluid Mech. 579, 1–28. http://dx.doi.org/10.1017/S0022112006003946.

Hutchins, N., Marusic, I., 2007b. Large-scale influences in near-wall turbulence. Philos. Trans. R. Soc. Lond. A Math. Phys. Eng. Sci. 365 (1852), 647–664. http://dx.doi.org/10.1098/rsta.2006.1942.

Jiménez, J., Pinelli, A., 1999. The autonomous cycle of near-wall turbulence. J. Fluid Mech. 389, 335–359. http://dx.doi.org/10.1017/S0022112099005066.

Lin, J., 2002. Review of research on low-profile vortex generators to control boundary-layer separation. Prog. Aerosp. Sci. (ISSN: 0376-0421) 38 (4), 389–420. http://dx.doi.org/10.1016/S0376-0421(02)00010-6, URL https://www.sciencedirect.com/science/article/pii/S0376042102000106.

Lögdberg, O., Fransson, J.H.M., Alfredsson, P.H., 2009. Streamwise evolution of longitudinal vortices in a turbulent boundary layer. J. Fluid Mech. 623, 27–58. http://dx.doi.org/10.1017/S0022112008004825.

Marusic, I., Heuer, W.D.C., 2007. Reynolds number invariance of the structure inclination angle in Wall turbulence. Phys. Rev. Lett. 99, 114504. http://dx.doi.org/10.1103/PhysRevLett.99.114504.

Marusic, I., Monty, J.P., 2019. Attached eddy model of wall turbulence. Annu. Rev. Fluid Mech. 51 (1), 49–74. http://dx.doi.org/10.1146/annurev-fluid-010518-040427.

Marusic, I., Monty, J.P., Hultmark, M., Smits, A.J., 2013. On the logarithmic region in wall turbulence. J. Fluid Mech. 716, R3. http://dx.doi.org/10.1017/jfm.2012.511.

Mathis, R., Hutchins, N., Marusic, I., 2009. Large-scale amplitude modulation of the small-scale structures in turbulent boundary layers. J. Fluid Mech. 628, 311–337. http://dx.doi.org/10.1017/S0022112009006946.

Mohammed-Taifour, A., Weiss, J., 2016. Unsteadiness in a large turbulent separation bubble. J. Fluid Mech. 799, 383–412. http://dx.doi.org/10.1017/jfm.2016.377.

Mole, A., Skillen, A., Revell, A., 2022. The interaction of longitudinal vortex pairs with a turbulent boundary layer. J. Fluid Mech. 953, A31. http://dx.doi.org/10.1017/jfm.2022.952.

Panton, R., 2001. Overview of the self-sustaining mechanisms of wall turbulence. Prog. Aerosp. Sci. (ISSN: 0376-0421) 37 (4), 341–383. http://dx.doi.org/10.1016/S0376-0421(01)00009-4, URL http://www.sciencedirect.com/science/article/pii/S0376042101000094.

Robinson, S.K., 1991. Coherent motions in the turbulent boundary layer. Annu. Rev. Fluid Mech. 23 (1), 601–639. http://dx.doi.org/10.1146/annurev.fl.23.010191.003125.

Rowley, C.W., Colonius, T., Murray, R.M., 2004. Model reduction for compressible flows using POD and Galerkin projection. Physica D. (ISSN: 0167-2789) 189 (1), 115–129. http://dx.doi.org/10.1016/j.physd.2003.03.001.

Sattarzadeh, S.S., Fransson, J.H.M., 2015. On the scaling of streamwise streaks and their efficiency to attenuate Tollmien–Schlichting waves. Exp. Fluids 56 (3), 1–16.

Sattarzadeh, S.S., Fransson, J.H.M., Talamelli, A., Fallenius, B.E.G., 2014. Consecutive turbulence transition delay with reinforced passive control. Phys. Rev. E 89, 061001. http://dx.doi.org/10.1103/PhysRevE.89.061001.

Schlatter, P., Li, Q., Brethouwer, G., Johansson, A.V., Henningson, D.S., 2010. Simulations of spatially evolving turbulent boundary layers up to $Re_\theta = 4300$. Int. J. Heat Fluid Flow (ISSN: 0142-727X) 31 (3), 251–261. http://dx.doi.org/10.1016/j.ijheatfluidflow.2009.12.011.

Schlatter, P., Stolz, S., Kleiser, L., 2004. LES of transitional flows using the approximate deconvolution model. Int. J. Heat Fluid Flow (ISSN: 0142-727X) 25 (3), 549–558. http://dx.doi.org/10.1016/j.ijheatfluidflow.2004.02.020, URL http://www.sciencedirect.com/science/article/pii/S0142727X04000281.

Shahinfar, S., Sattarzadeh, S.S., Fransson, J.H.M., 2014. Passive boundary layer control of oblique disturbances by finite-amplitude streaks. J. Fluid Mech. 749, 1–36. http://dx.doi.org/10.1017/jfm.2014.211.

Shahinfar, S., Sattarzadeh, S.S., Fransson, J.H.M., Talamelli, A., 2012. Revival of classical vortex generators now for transition delay. Phys. Rev. Lett. 109, 074501. http://dx.doi.org/10.1103/PhysRevLett.109.074501.

Smits, A.J., McKeon, B.J., Marusic, I., 2011. High–Reynolds Number Wall turbulence. Annu. Rev. Fluid Mech. 43 (1), 353–375. http://dx.doi.org/10.1146/annurev-fluid-122109-160753.

Stolz, S., Adams, N.A., Kleiser, L., 2001. An approximate deconvolution model for large-eddy simulation with application to incompressible wall-bounded flows. Phys. Fluids 13 (4), 997–1015. http://dx.doi.org/10.1063/1.1350896.

Tomkins, C.D., Adrian, R.J., 2003. Spanwise structure and scale growth in turbulent boundary layers. J. Fluid Mech. 490, 37–74. http://dx.doi.org/10.1017/S0022112003005251.